International Journal of Nanomedicine

Dovepress
open access to scientific and medical research

Open Access Full Text Article

ORIGINAL RESEARCH

Targeted Therapy of Atherosclerosis Vulnerable Plaque by ROS-Scavenging Nanoparticles and MR/Fluorescence Dual-Modality Imaging Tracing

Yue Dai[1,2,*], Xuan Sha[1,*], Xiaoxi Song[1], Xiuli Zhang[1,2], Mengyuan Xing[1], Siwen Liu[1], Kai Xu[1,2], Jingjing Li[1,2]

[1]School of Medical Imaging, Xuzhou Medical University, Xuzhou, 221004, People's Republic of China; [2]Department of Radiology, Affiliated Hospital of Xuzhou Medical University, Xuzhou, 221006, People's Republic of China

*These authors contributed equally to this work

Correspondence: Kai Xu; Jingjing Li, Email xkpaper@163.com; qingchao0124@163.com

Purpose: Early diagnosis and treatment of atherosclerosis (AS) vulnerable plaque has important clinical significance for the prognosis of patients. In this work, the integrated diagnosis and treatment nanoparticles based on Gd-doped Prussian blue (GPB) were constructed for the fluorescence/MR dual-mode imaging and anti-ROS treatment of vulnerable AS plaques in vitro and in vivo.

Methods: To fabricate the theranostic NPs, GPB was modified with water-soluble polymer polyethyleneimine (PEI), fluorescence molecule rhodamine (Rd), and targeted molecule dextran sulfate (DS) step by step via electrostatic adsorption to construct GPRD NPs. The fluorescence/MR imaging ability and various nano-enzymes activity of GPRD NPs were detected, and the biocompatibility and safety of GPRD were also evaluated. Subsequently, RAW264.7 cells and ApoE -/- model mice were used to evaluate the effect of GPRD NPs on the targeted dual-mode imaging and anti-ROS treatment of vulnerable plaque in vitro and in vivo.

Results: The experimental results showed that our fabricated GPRD NPs not only displayed excellent MR/fluorescence dual-modality imaging of vulnerable plaque in vivo but also effectively utilized the nano-enzyme activity of GPB to inhibit the AS progress by ROS scavenging and the following reduction of inflammation, apoptosis, and foam cells' formation, providing a new avenue for the diagnosis and treatment of AS vulnerable plaque.

Conclusion: The fabricated multimodal imaging nanoparticles with ROS-scavenging ability provided a new avenue for the diagnosis and treatment of AS vulnerable plaques.

Keywords: vulnerable plaques, ROS scavengers, nano-enzyme, MRI, fluorescence imaging

Introduction

Atherosclerosis (AS) vulnerable plaque is a kind of unstable high-risk plaque. Due to the structure and pathological basis of vulnerable plaques, they are unstable and easy to rupture to form thrombus, leading to the occurrence of acute cardiovascular and cerebrovascular events, as well as further clinical adverse events such as acute myocardial infarction, cardiac arrest, acute cerebral infarction and so on.[1,2] Therefore, early identification and treatment of vulnerable plaque are more meaningful to improve the prognosis of patients.

Up to now, a series of strategies have been developed for the targeted detection and treatment of vulnerable AS plaques. Wang et al engineered a sensitive, specific and biocompatible molecular probe for dual-modality imaging of macrophages within atherosclerotic lesions, which could be effectively internalized by vulnerable plaques because of its high affinity for macrophage scavenger receptor class A (SR-A).[3] Tong Wei et al engineered a novel multimodal imaging agent, 5-HT-Fe_3O_4-Cy7 nanoparticles used for active myeloperoxidase (MPO) targeting, by conjugating superparamagnetic iron oxide nanoparticles (SPIONs) with 5-hydroxytryptamine and cyanine 7 N-hydroxysuccinimide ester.[4] Ma et al developed a nanocomplex (ICG/SRT@HSA-pept NMs) for targeted treatment

Received: 22 April 2022
Accepted: 8 November 2022
Published: 17 November 2022

Graphical Abstract

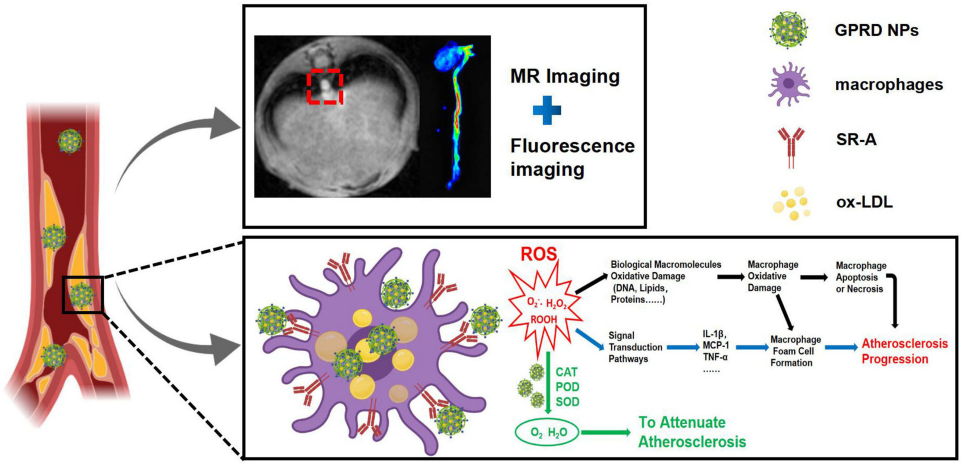

of atherosclerotic plaque, where SRT1720 acted as a therapeutic drug. In their nanoformulation, osteopontin (OPN) was selected as the targeting molecule for vulnerable atherosclerotic plaques.[5] Manse Kim et al developed cRGD-conjugated pluronic nanocarrier, loading with a multipotent anti-inflammatory cytokine, interleukin-10 (IL10). The fabricated nanomaterials could bind with $\alpha_v\beta_3$ integrin, which was overexpressed in the neovasculature of the vulnerable plaque to realize the targeted treatment of atherosclerotic plaques.[6,7] Although well documented, more works are still needed to address the remaining issues, such as the early recognition of vulnerable plaques, controlled drug releasing and the avoid of complex structure and complicated preparation of nanocomplex, which hamper their further clinical transformation.

Thus, in this work, we aim to develop a novel theranostic nanoplatform that can specifically recognize and inhibit the progress of vulnerable AS plaque in a relatively easy way. AS is a kind of common chronic inflammatory vascular wall disease, which is often accompanied by the production of reactive oxygen species (ROS) in its occurrence and development. ROS can lead to macrophages activation, cell apoptosis, and oxidative damages to biomacromolecules (such as lipid, protein, DNA, etc).[8,9] ROS and its oxidation products can activate the corresponding signaling pathways with functional signaling molecules, which mediate a series of changes in vascular cells and affect vascular function and normal structure.[10] Based on the crucial role of ROS in the pathogenesis of AS, eliminating ROS might be an important strategy for AS treatment. Aiming to inhibit AS progress by ROS scavenging, we turned our attention to Prussian blue (PB). Learned from the literature,[11–13] PB has catalase (CAT), peroxidase (POD), superoxide dismutase (SOD), and other enzyme activities, which can effectively remove ROS in lesions and relieve oxidative response and inflammation.[14–17] The nano-enzyme effect of PB has been used in the treatment of inflammatory bowel disease and stroke injury, which has achieved remarkable therapeutic effect.[18–20] It is more important that PB is of interest due in part to its excellent biocompatibility,[21] which is approved by the US Food and Drug Administration (FDA), under the brand name Radiogardase®, for treatment of patients with contamination of cesium and/or thallium.[22]

Here, we develop a PB NPs-based theranostic nanocomplex for the diagnosis and treatment of vulnerable AS plaque by ROS scavenging and MR/fluorescence imaging. Gd-doped PB (GPB) as a multifunctional nanocarrier for MRI and ROS scavenging was first prepared by a one-step hydrothermal method. Then, GPB was further modified with water-soluble polymer polyethyleneimine (PEI), fluorescence molecule rhodamine (Rd), and targeted molecule dextran sulfate (DS) which is one of the excellent ligands of SR-A[23–25] step by step via electrostatic adsorption. The experimental results showed that our fabricated GPB-PEI-Rd-DS nanoparticles (GPRD NPs) not only displayed excellent MR/fluorescence dual-model imaging of AS vulnerable plaque in vivo but also effectively inhibited the AS progress at the same time by

utilizing the nano-enzyme ability of GPB for ROS scavenging and the following reduction of inflammation, apoptosis, and foam cells' formation. Such theranostic nanoparticles might provide a new avenue for the recognition and treatment of AS vulnerable plaque in a relatively easy way.

Materials and Methods

Materials

Polyvinylpyrrolidone (PVP, K30), potassium ferricyanide ($K_3[Fe(CN)_6]$), gadolinium nitrate hexahydrate [$Gd(NO_3)_3{\cdot}6H_2O$] and Rhodamine 6G were purchased from Dalian Meilun Biotechnology Co., LTD (Dalian, China). Polyethyleneimine (PEI) was obtained from Aladdin Chemical Reagent Co., Ltd. Dextran sulfate (DS) and Oil Red O stain kit were obtained from Solarbio Chemical Reagent Co., Ltd. Reagents for cell cultures including fetal bovine serum, trypsin, and DMEM were supplied by Gibco (Thermo Fisher Scientific Co., Ltd., Shanghai, China). The TNF-α, IL-1β and MCP-1 ELISA Kits were purchased from Solarbio Chemical Reagent Co., Ltd (Beijing, China). Total Cholesterol (TC) Content Assay Kit was purchased from Shanghai Cablebridge Biotechnology Co., Ltd (Shanghai, China). SOD Activity Assay Kit was received from Shanghai BestBio Biological Reagent Co., Ltd (Shanghai, China). Annexin V-FITC/PI cell apoptosis assay kit was obtained from Jiangsu Keygen Biotechnology Co. Ltd (Nanjing, China). ROS Fluorescent Probe-DCFH-DA was purchased from Dalian Meilun Biotechnology Co., LTD (Dalian, China). Oxidized low-density lipoprotein was received from Shanghai Yuanye Biotechnology Co., Ltd (Shanghai, China). All aqueous solutions were prepared with ultrapure water (≥18 MΩ, Milli-Q, Millipore).

Preparation of GPRD NPs

GPB nanoparticles were synthesized according to the literature with some modifications.[26] In brief, 32 mg $K_3[Fe(CN)_6]$ and 1 g PVP were added into 10 mL HCl solution (0.01 M) to obtain a clear solution A by stirring. One gram of PVP and 60 mg $Gd(NO_3)_3{\cdot}6H_2O$ were added to 10 mL HCl solution (0.01 M) to obtain a clear solution B. Subsequently, solution A and solution B were slowly mixed with magnetic stirring for 3 h and the mixed solution was placed in an oven at 80°C for 24 hours. After centrifugation at 16,000 rpm for 30 min, the precipitate was washed thrice with distilled water and once with ethanol to obtain GPB nanoparticles.

Then, 2 mL PEI aqueous solution (10 mg/mL, pH = 5.0) was added slowly into 2 mL of GPB (5 mg/mL). The obtained solution was stirred at 1000 rpm for 4.[27,28] After centrifugation at 14,000 rpm for 30 min, GPB-PEI were washed with distilled water thrice and freeze-dried. GPRD NPs were then prepared via electrostatic absorption. In brief, 1 mL DS (10 mg/mL) and 1 mL Rd (0.5 mg/mL) were added slowly to 1 mL GPB-PEI (1 mg/mL), and the mixture was stirred under an ice rocker for 4 h. After centrifugation at 13,000 rpm for 30 min, the precipitate was washed with distilled water three times to obtain GPRD NPs.

Characterization of GPRD NPs

The morphology, size, and composition of the GPRD NPs were characterized by transmission electron microscopy (TEM, TEC-NAI G2, USA) and EDS-mapping. A DSL analyzer (Zetasizer Nano ZS90) was used to measure the size distribution and zeta potential during the preparation. The UV-vis absorption spectra of the GPB, Rd, and GPRD NPs were recorded by a HITACHI UH4150 Spectrophotometer (HITACHI, Japan). The absorbance peaks of GPB and DS were detected by a Fourier infrared spectrometer (FT-IR, Bruker, Germany). The concentration of gadolinium in GPB and GPRD NPs was determined by inductively coupled plasma-optical emission spectroscopy (ICP-MS, Thermal Elemental). The fluorescence emission of GPRD NPs was measured by LS55 Fluorescence Spectrometer (PerkinElmer, America). The 3.0T MR imaging system (GE discovery 750W) with a small animal coil was used to measure the MR signal value of GPRD. The particle size, fluorescence, and MRI signal intensity of GPRD NPs were measured at 0, 1, 3, 5, and 7 days to demonstrate the stability of GPRD NPs.

T_1 Relaxivity Measurements of GPB and GPRD NPs

The T1-weighted relaxivity of GPB and GPRD NPs was determined under a 3.0 T MR system. T_1 images of GPB and GPRD NPs suspensions with different concentrations were obtained by 3.0 T MRI. The scanning parameters were set as follows: Field of view = 18 cm×18 cm, TE = Min Full, TR = 425 ms, Matrix size = 384 × 224, Slice spacing = 1.5 mm, Slice thickness = 3.0 mm.

Determination of ROS-Scavenging Capability

Different concentrations of GPRD NPs (0, 10, 30, 50, 80, 100 μg/mL) were cultured in 2 mL 0.01 M PBS (pH = 7.4) containing 500 mM H_2O_2 for 2 h to evaluate their ability of H_2O_2 scavenging. Subsequently, the residual H_2O_2 was measured by a UV-vis-NIR spectrometer at 240 nm. In addition, 100 μg/mL of GPRD NPs were added into 2 mL of 0.01 M PBS (pH = 7.4) containing 500 mM H_2O_2 for different times (from 0 to 4 h), and the residual H_2O_2 amount was measured similarly. The eliminated H_2O_2 amount was calculated accordingly (n = 3).

Commonly used natural POD substrate, 3,5,3',5'-tetramethylbenzidine (TMB) was selected as a substrate to investigate the POD activity of GPRD NPs. Then, 30% H_2O_2, 10 mg/mL TMB and GPRD NPs with different concentrations were added to the buffer solution (pH = 5.0) to observe the color change (GPRD:H_2O_2:TMB:buffer = 1:3:1:20). The POD-like activity of GPRD NPs was evaluated by recording the absorption value at 650 nm of the oxidation state TMB generated in the reaction system with a UV spectrophotometer. Also, the absorption values at 650 nm of the oxidation state TMB at different time points were recorded (n = 3).

SOD activity of GPRD NPs with different concentrations (10, 30, 50, 80, 100 μg/mL) was determined by a SOD Assay kit (BestBio, Shanghai) according to the introduction (n = 3). The CAT, POD and SOD abilities of GPB, GPB-PEI and GPR were evaluated with the same operation.

Cell Culture

RAW264.7 macrophages and human umbilical vein endothelial cells (HUVEC) were purchased from the Cell Bank of the Chinese Academy of Sciences (Shanghai, China). RAW264.7 cells were cultured in a DMEM medium (Gibco) containing 10% FBS, 1% penicillin (100 mg mL^{-1}), and streptomycin (100 mg mL^{-1}). HUVEC cells were propagated in RPMI 1640 medium (Gibco) containing 10% FBS-containing, 1% penicillin (100 mg mL^{-1}), and streptomycin (100 mg mL^{-1}). All cells were cultured in a 5% CO_2 saturated humidity incubator at 37 °C.

Cell Cytotoxicity Evaluation

In this study, MTT assays were employed to evaluate the cytotoxicity of GPRD NPs in vitro. Briefly, RAW264.7 and HUVEC cells (1×10^5 cells each well) were cultured in 96-well plates for 24 h at 5% CO_2, 37 °C (n = 6). Then, 100 μL fresh medium containing different concentrations of GPRD NPs (0, 10, 30, 60, 90, 150, 200, 300, 400 μg/mL) was introduced to replace the culture medium and incubated for another 24 hours. After removing GPRD NPs and washing with PBS buffer, DMEM containing 1 mg/mL MTT was added to each well and cultured for 4 h. The medium was then removed and 100 μL of dimethyl sulfoxide (DMSO) was added to dissolve formalin crystals for another 15 minutes. The absorbance at 490 nm was measured by a microplate reader (Multiskon MK3, USA).

Cell Uptake and Targeted Fluorescence Imaging

To study the possibility of targeted imaging with GPRD to activated macrophages, the overexpression of SR-A in activated macrophages was first evaluated by Western Blot (WB) assay. The RAW 264.7 cells incubated with the fresh medium were used as the control group, and the macrophages treated with medium containing lipopolysaccharide (LPS) were used as model cells. After 12 h, the cells in two groups were collected for the WB assay.

The targeting ability of GPRD NPs towards the activated RAW264.7 cells was observed by confocal laser scanning microscopy (CLSM). RAW264.7 cells were cultured in 6-well plates (1×10^5 cells per well) and incubated for 12 h with or without LPS stimulation (n = 3). Then, they were incubated with GPRD NPs and GPR NPs at 10 μg/mL, respectively. After 20 minutes of culture, RAW264.7 cells were washed and stained with DAPI. The fluorescence images of treated

cells were obtained by CLSM. Similarly, cell internalization was also studied at different times (10, 20, 40, 90 min) and different doses of GPRD NP (10, 30, 50 μg/mL). To further inspect the specificity of the cell targeting, CD204 antibody was employed to block the scavenger receptor A on RAW264.7 cell surface before the addition of GPRD NPs. Other steps were kept the same.

To compare the cellular uptake of NPs (GPB, GPB-PEI, GPR, GPRD, CD204 + GPRD) by RAW264.7 cells (LPS-/+), the cells were treated with different NPs (GPB, GPB-PEI, GPR, GPRD, CD204 + GPRD) at 50 μg/mL for 4 h, respectively. After discarding the NPs, RAW264.7 cells were washed, trypsinized, centrifuged, counted and dissolved in HNO_3 for ICP-MS determination (n = 3).

Targeted MR Imaging in vitro

RAW264.7 cells were cultured in 6-well plates (1×10^5 cells per well) and incubated for 12 h with or without LPS stimulation. Then, the cells were incubated with GPRD NPs or GPR NPs at 50 μg/mL, respectively. Subsequently, the cells were washed with PBS, trypsinized and centrifuged. The collected cells were resuspended and solidified with 300 μL 1% agarose solution for MRI on a 3.0 T MR scanner.

Intracellular ROS Generation

RAW264.7 cells were cultured in 6-well plates with a density of 1×10^4 per well overnight. The cells in the control group were cultured in the fresh medium, and those in the model group were activated with LPS (10 ng/mL) for 30 min. Then, the cells in the two groups were incubated with GPRD NPs or GPR NPs with a concentration of 50 μg/mL for 4 h, respectively. Afterward, cells were rinsed and treated with 2,7-dichlorodi-hydrofluorescein diacetate (DCFH-DA, 10 μM) in PBS for 30 min. After washing with PBS, the production of intracellular ROS in cell culture medium was observed by Inverted Fluorescence Microscope.

Intracellular Inflammatory Cytokines Measurement

RAW264.7 cells were cultured in 12-well plates with a density of 1×10^5 per well and incubated overnight. The cells in the control group were cultured in the fresh medium, and those in the model group were activated with LPS (10 ng/mL) for 30 min. Then, the cells in two groups were incubated with GPRD NPs or GPR NPs with a concentration of 50 μg/mL for 24 h. Afterward, supernatants in all groups were harvested and assayed for IL-1β, MCP-1, and TNF-α using corresponding ELISA kits (n = 6).

Inhibition of Foam Cell Formation

The foam cell formation was evaluated by the determination of intracellular TC levels and Oil Red O staining. Briefly, RAW264.7 cells were cultured in 6-well plates (1×10^5 per well) and incubated overnight. Cells in the control group were cultured in the fresh medium, and those in the other groups (model group, GPR group and GPRD group) were stimulated with LPS for 12 h. GPRD NPs or GPR NPs (50 μg/mL) were introduced in GPR group and GPRD group for 2 h incubation, respectively. After discarding the NPs, 50 μg/mL ox-LDL was added to all four groups and co-incubated for 48 h. Subsequently, RAW264.7 with different treatments were stained with Oil Red O staining for 40 min and rinsed carefully three times with double distilled water for the observation under optical microscope. Parallelly, the TC levels of RAW264.7 with different treatments were detected by TC assay kits.

Anti-Apoptosis Activity of GPRD NPs in Macrophages

RAW264.7 cells were cultured in 6-well plates with a density of 1×10^5 cells per well. After 12 h, 50 μg/mL GPRD NPs or GPR NPs were added to GPRD group and GPR group for another 2 h incubation, respectively. Then, fresh medium containing 200 μM H_2O_2 was added to the cells and cultured for 24 h. The cells in the model group were incubated with fresh medium containing 200 μM H_2O_2 for 24 h and those in the control group were only incubated with fresh medium. Finally, the cells were collected and stained with an annexin V-FITC/PI apoptosis detection kit to assay the apoptosis via flow cytometry.

Animal Experiments

Animal experiments were conducted according to the guidelines of the National Institutes of Health on the use of animals in research. All animal experiments were approved by the Animal Care Committee of Xuzhou Medical University (L20210226113). C57BL/6 mice (female, 6 weeks old) and Apolipoprotein E-deficient (ApoE -/-) mice (female, 6 weeks old) were obtained from the Animal Center of Xuzhou Medical University. ApoE -/- mice were given a high-fat diet containing 21.2% lard, 49.1% carbohydrate, 19.8% protein, and 0.2% cholesterol for 2 months to construct animal models of atherosclerosis.

In vivo Safety Evaluation

As mentioned, the hemolysis of GPRD nanoparticles was detected by direct contact method in vitro.[29,30] One milliliter of mouse blood was washed three times with 1.25 mL of isotonic sodium chloride solution. Two hundred microliters of red blood cells was diluted with 10 mL of isotonic sodium chloride solution. Then, 0.1 mL of diluted blood samples was added to GPRD NPs solutions with different concentrations (10, 50, 100, 150, 200, 300, 400, 500 μg/mL) for 1 h culture at 37 °C. Then, the solutions were centrifuged at 3000 rpm for 5 min. The absorbances of the supernatants were measured at 540 nm by a microplate reader to determine the hemoglobin released by dissolved red blood cells. The diluted blood samples incubated with isotonic sodium chloride solution and double distilled water were used as negative and positive controls, respectively.

In vivo toxicity study was conducted on C57BL/6 mice (female, 6 weeks). Mice were randomly divided into two groups and then post-injected with normal saline and GPRD NPs (10 μmol/kg Gd) via tail vein, respectively. Blood samples were collected at 1st, 7th, and 21st days after injection for biochemical analysis and routine blood analysis. At the end of the experiment, the heart, liver, spleen, kidney, and lung were collected, fixed with 10% formalin, sectioned, and stained with H&E for histological analysis. Finally, the histological samples were observed using an optical microscope.

The Expression of SR-A in the Plaque of ApoE -/- Mice

ApoE-/- mice were given a high-fat diet for 2 months. The aortas were dissected and the thoracic aortas were selected. The sections were fixed in ice-cold acetone for 5 min and then blocked with goat serum. Subsequently, the sections were labeled with anti-mouse SR-A monoclonal antibody overnight and labeled with pink-conjugated secondary antibody for 1 h. Finally, the sections were stained with DAPI and fixed for CLSM observation. Flow cytometry was also employed to verify the expression of SR-A in aortic plaques of model ApoE-/- mice. The cells of aortic plaques were co-incubated with CD204 antibody labeled with PE to evaluate the expression of SR-A in plaque lesions by flow cytometry.

In vivo Targeting Performance

Immunofluorescence analysis was carried out to confirm the targeting ability of GPRD NPs against vulnerable plaques. The ApoE -/- plaque-bearing mice were injected with GPRD NPs or GPR NPs (10 μmol/kg Gd) through the tail vein, respectively. Two hours later, the aortas were dissected and the thoracic aortas were selected. The sections were fixed in ice-cold acetone for 5 min and then blocked with goat serum. Subsequently, the sections were labeled with anti-mouse SR-A monoclonal antibody overnight and labeled with pink-conjugated secondary antibody for 1 h. Finally, the sections were stained with DAPI and fixed. The fluorescence imagings of DAPI, SR-A, GPR and GPRD NPs were obtained by confocal laser scanning microscope.

In vivo Targeted Imaging

The ApoE -/- plaque-bearing mice were injected with GPRD NPs or GPR NPs (10 μmol/kg Gd) for in vivo MR imaging. The images were performed on a 3.0 T MR scanner pre- and post-administration at various time points (0.5, 2, 6, 12, 24 h).

The ApoE -/- plaque-bearing mice were injected with GPRD NPs or GPR NPs (10 μmol/kg Gd) for in vivo fluorescence imaging. Two hours later, the aorta and major organs were dissected and fluorescence images were captured using an in vivo imaging system.

In vivo Targeted Treatment

The ApoE -/- mice were divided into four groups: (a) control group, (b) model group, (c) GPR NPs group and (d) GPRD NPs group (n = 6). The mice in the control group were fed normal diets and the mice in the other three groups were fed with high-fat diets for 2 months. Then, the mice in group c and d were administered with 200 μL GPR NPs (10 μmol/kg Gd) or GPRD (10 μmol/kg Gd) intravenously, whereas those in group b were administered with 200 μL of saline intravenously. Mice were treated twice a week and their body weights were recorded once a week. Five weeks later, all mice were euthanized, and the aortas were collected for Oil Red O staining to evaluate the efficacy of different treatments and quantify by ImageJ.

For histological analysis, thoracic aortas of four groups were collected for H&E staining. For immunohistochemistry analysis, sections of thoracic aorta were incubated with antibodies, including CD68, MMP-9, and α-SMA, respectively.

Statistical Analysis

Statistical analysis was performed using SPSS 19.0 software. All data in this study were expressed as mean value ± SD. One-way ANOVA and Dunnett test were employed for comparison between multiple samples. The Student *t*-test was adopted to evaluate the statistical significance between two groups. The data of each group were statistically analyzed to obtain the corresponding P-value. In all cases, $P < 0.05$ was considered statistically significant. The smaller the P-value, the more significant the difference between the groups and $^{***}P < 0.001$ showed the experimental data have strong statistical power.

Results and Discussion

Preparation and Characterization of GPRD NPs

Gd-doped GPB was prepared by a one-step hydrothermal method with a simple and stable structure (Figure 1A). TEM images demonstrated the formation of uniform GPB and GPRD NPs with cube morphology. The average sizes were 88.7 ± 6.3 and 99.4 ± 6.7 nm for GPB and GPRD NPs, respectively (Figure 1B). Element mapping confirmed the composition of GPRD NPs with C, N, Fe, Gd, and K elements (Figure 1C), and the five elements were distributed uniformly in the structure of GPRD NPs. As shown in Figure 1D, the hydrodynamic diameter was increased accordingly after each step of assembly. They were 142 nm for GPB, 190 nm for GPB-PEI, and 220 nm for GPRD NPs. In addition, the zeta potential change also witnessed this assembly process. The potential value of GPB was −14.4 mV, and after PEI assembly, it was changed to 29.4 mV due to the positively charged PEI. With the addition of DS and Rd, the zeta potential of the GPRD NPs became −25.6 mV (Figure 1E). Fourier transform infrared spectroscopy (FT-IR) of GPRD NPs showed the typical absorbance peaks of −CN− stretching of GPB and S=O stretching of DS at approximately 2089 and 1262 cm^{-1} (Figure 1F), respectively, indicating the successful assembly of DS. The UV−vis−NIR absorbance spectrum of GPRD NPs discovered an obvious characteristic GPB peak at 706 nm and the red-shift absorbance spectrum from 527 nm to 553 nm (Figure 1G), coming from the Rd coating. The above results proved the successful synthesis of GPRD NPs well.

Dual-Modality Imaging and Stability Features of GPRD NPs

To be used as a dual-model contrast agent, the MRI and fluorescence imaging ability of GPRD NPs were first evaluated. AS shown in Figure 1H, GPRD NPs solution emitted a bright yellow-green light upon irradiation with a UV lamp (365 nm). The emission wavelength of GPRD NPs was 550 nm with an excitation wavelength of 490 nm. Furthermore, as the concentration of GPRD NPs increased, the fluorescence intensity displayed a gradual increase. The MR images of GPRD NPs were conducted by a previously described MR system. As shown in phantom images and pseudo-color images (Figure 1I), the MR signal intensity of GPB and GPRD NPs increased along with the increase in Gd concentration, and

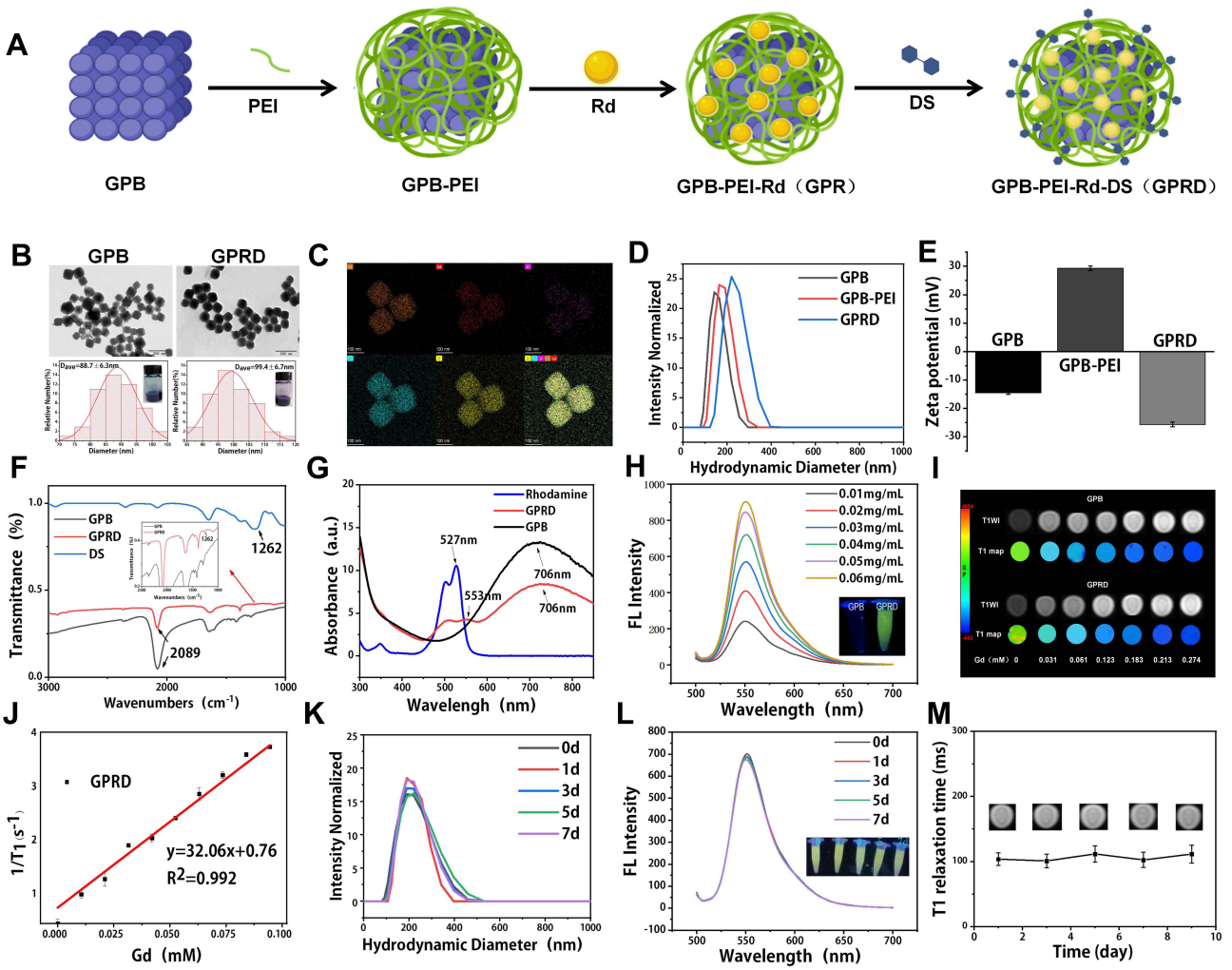

Figure 1 (**A**) Schematic illustration of the fabrication of GPRD NPs. (**B**) TEM image and size distribution profile of GPB and GPRD NPs. (**C**) Corresponding STEM-EDS elemental mappings of GPRD NPs. Characterization of the assembly process of GPRD NPs with hydrodynamic diameter (**D**) and zeta potential determination (**E**). (**F**) FT-IR spectra of GPB (black line), DS (blue line), and GPRD NPs (red line). (**G**) The UV-Vis spectra of GPB (black line), Rhodamine (blue line), and GPRD NPs (red line). (**H**) The photoluminescence emission of GPRD NPs with different concentrations with a excitation wavelength of 490 nm. (**I**) T_1-weighted MR images of GPB and GPRD NPs with different concentrations. r_1 relaxivity curves of GPRD NPs (**J**). The stability characterizations of GPRD NPs with hydrodynamic diameter (**K**), fluorescence intensity (**L**), and MRI T_1 signal intensity (**M**).

the T_1 relaxivity (r_1 value) of GPRD NPs were calculated to be 32.06 mM^{-1} s^{-1} (Figure 1J). The T_1 relaxivity of GPRD NPs was probably 8 times comparing with that of Gd-DTPA (4.21 mM^{-1} s^{-1}),[31] indicating an enhanced MR contrast ability of GPRD NPs.

The prepared GPRD NPs should possess good physiological stability for their biomedical application. Thus, we investigated the colloid stability of GPRD NPs by determining the changes of hydrodynamic diameter with the time passing. As shown in Figure 1K, their hydrodynamic diameters kept stable at about 220 nm in PBS buffer without significant changes for even 7 days standing. More importantly, no noticeable signal changes of fluorescence and MR intensities were observed during the 7 day-period (Figure 1L and M), demonstrating the good stability of GPRD NPs in aqueous conditions.

ROS-Scavenging Capacity of GPRD NPs

PB was reported to possess the ability to eliminate ROS,[32] and act as a variety of nano-enzymes to limit tumor and inflammation.[33–35] We suspected that GPRD NPs should preserve the ROS-scavenging capacity of PB, which could be used for the inhibition of AS plaque progress. Therefore, their catalase (CAT)-like, peroxidase (POD)-like, and

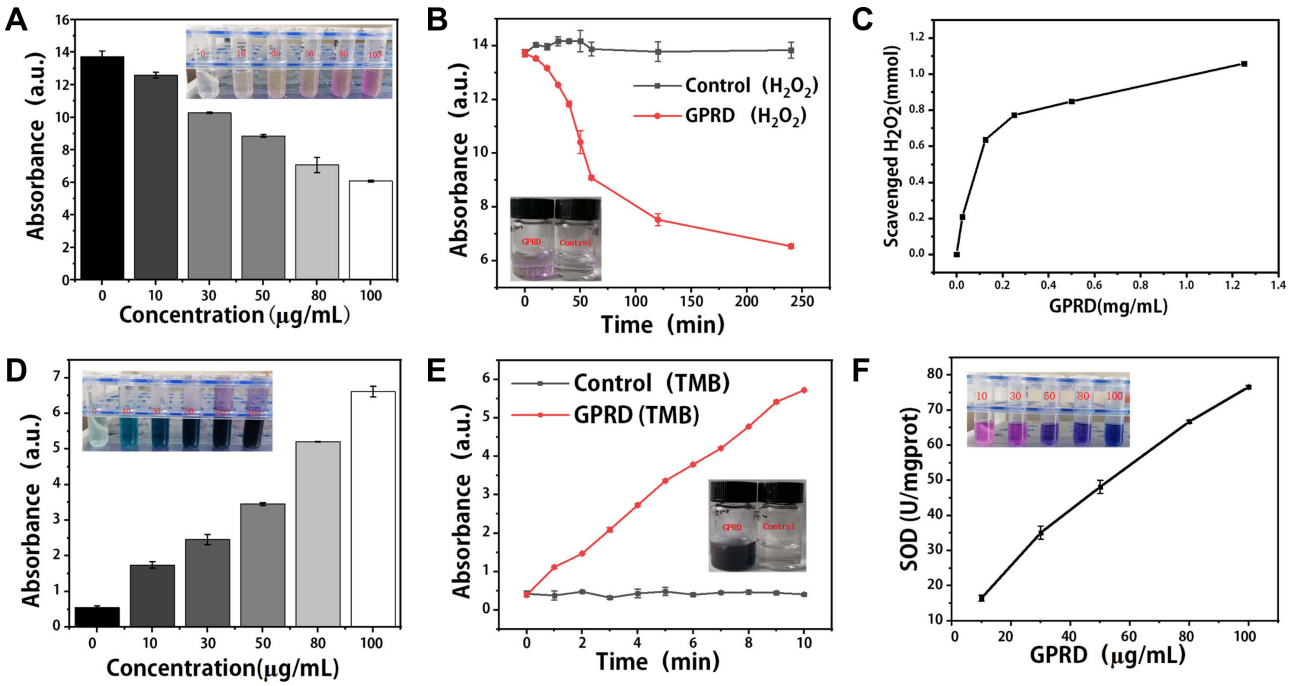

Figure 2 Measurement of CAT-like activity of GPRD NPs with different concentrations (**A**) and different time points (**B**). (**C**)The capacity of GPRD to remove H_2O_2 in a dose-dependent profile. Measurement of POD-like activity of GPRD NPs with different concentrations (**D**) and different time points (**E**). (**F**) Evaluation of the SOD-like enzyme activity of GPRD.

superoxide dismutase (SOD)-like activities of GPRD NPs were first evaluated. As shown in Figure 2A, the addition of H_2O_2 into the GPRD NPs solution generated a number of observable bubbles, which were verified to be O_2 by a dissolved oxygen electrode. It might be attributed to the decomposition of H_2O_2 into H_2O and O_2 by the CAT-like activity of GPRD NPs. Moreover, GPRD NPs induced H_2O_2 consumption displayed a time- and concentration-dependent manner (Figure 2A-C). The CAT-like activity can be shown in the following reaction.

$$H_2O_2 \rightarrow O_2 + H_2O$$

Then, we further studied the POD-like activity of GPRD NPs. A commonly used natural POD substrate, TMB, was selected to investigate their POD-like activity. The absorbance of TMB (oxidized) at 650 nm was recorded with a Microplate Reader. As shown in Figure 2D and E, the absorbance was increased with the addition of GPRD NPs, indicating GPRD NPs could catalyze H_2O_2 to oxidize the toxic TMB into nontoxic substances. Furthermore, such oxidation was also concentration- and time-dependent. The POD-like activity can be shown in the following reaction.

$$TMB + H_2O_2 + H^+ \rightarrow TMB_{(oxidized)} + H_2O$$

Lastly, we evaluated the $O_2{\cdot}^-$-scavenging capability of GPRD NPs by SOD-like activity. We used the xanthine/xanthine oxidase system to induce the generation of $O_2{\cdot}^-$ by SOD Assay kit. The absorbance of 550 nm was recorded after the addition of the GPRD NPs into the xanthine/xanthine oxidase system 45 min later. With the $O_2{\cdot}^-$-scavenging, the color of the reaction solution became lighter due to the nitrite reduction, which indicates a high $O_2{\cdot}^-$ -scavenging capacity of GPRD NPs (Figure 2F). Moreover, GPRD NPs eliminated $O_2{\cdot}^-$ in a dose-dependent profile. The SOD-like activity can be shown in the following reaction.

$$2O_2{\cdot}^- + 2H+ \rightarrow H_2O_2 + O_2$$

Hence, the above results suggested that the prepared GPRD NPs can act as nano-enzymes to efficiently change the detrimental ROS into H_2O and O_2, possessing the potentials to avoid oxidative damages to biomacromolecules and block some ROS mediated inflammatory signaling pathways. Meanwhile, we further compared these nano-enzyme abilities of GPB, GPB-PEI, GPR, and GPRD. As expected, there was no significant difference in their nano-enzyme activities which came from their common component, PB (Figure S1). Studies have shown that PB NPs have CAT-like, SOD-like, and

POD-like activities, which were caused by the abundant redox potentials of their different forms, making them efficient electron transporters.[14] We believe that GPRD NPs have great potential for the treatment of oxidative stress in vulnerable atherosclerotic plaques.

GPRD NPs Enhance ROS-Scavenging and Anti-Inflammatory Effect in Activated RAW264.7 Cells

AS mentioned above, ROS play a crucial role in the pathogenesis of AS and ROS scavenging might be an effective strategy for AS treatment. The good CAT-like, SOD-like, and POD-like activities of GPRD NPs inspired us to further study whether GPRD NPs can inhibit ROS generation in activated RAW264.7 cells. As expected, LPS-treated RAW264.7 cells produced more ROS, presenting a stronger green fluorescence signal in cells (Figure 3A and B, control and model group). After the introduction of GPR NPs and GPRD NPs, the green fluorescence emissions from ROS were reduced and the presence of DS in GPRD NPs

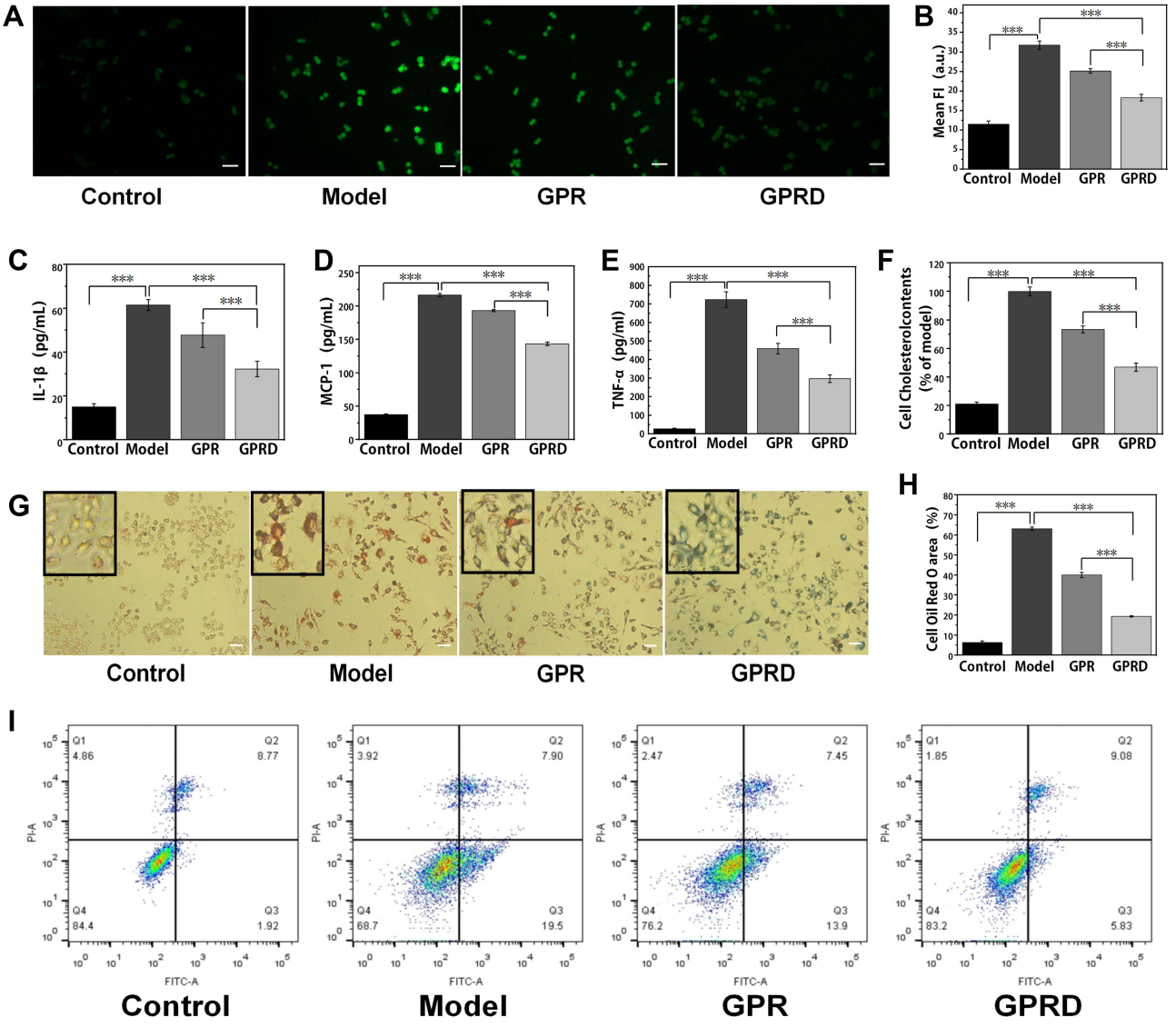

Figure 3 (**A** and **B**) Fluorescence images showing the intracellular ROS generation after treatment with GPR NPs and GPRD NPs and the quantitative analysis. (**C-E**) Typical inflammatory cytokines IL-1β, MCP-1, and TNF-α secreted by RAW264.7 cells by ELISA after different treatments. (**F**) The level of total cholesterol in RAW264.7 cells after different treatments. (**G** and **H**) Optical microscopy images showing oxLDL-induced foam cell formation in macrophages cells and the quantitative analysis. The insets in g were the local magnifications. (**I**) Inhibiting the apoptosis of RAW264.7 induced by H_2O_2 after different treatments. Scale bar = 50 μm and ***$P < 0.001$.

Abbreviations: Control, RAW264.7 cells without LPS (unactivated cells); Model, RAW264.7 cells with LPS (activated cells); GPR, activated RAW264.7 cells co-incubation with GPR NPs; GPRD, activated RAW264.7 cells co-incubation with GPRD NPs.

favored such ROS clearance more effectively, showing the strong inhibition ability of GPRD NPs in ROS production in activated RAW264.7 cells (***$P < 0.001$) (Figure 3A and B, GPR and GPRD group).

AS is a chronic inflammatory disease and ROS overexpressed in activated macrophages in vulnerable plaque involves inflammatory signal transmission pathways to produce excessive inflammatory factors, such as IL-1β, MCP-1, and TNF-α. The ROS-scavenging ability of GPRD NPs stimulated us to evaluate whether GPRD NPs could indirectly reduce the production of inflammatory cytokines. As shown in Figure 3C-E, compared with the control group, inflammatory cytokines (IL-1β, MCP-1, and TNF-α) were all overproduced from LPS stimulated RAW264.7 cells (model group). With the further treatment of GPR NPs or GPRD NPs, the overproduced inflammatory cytokines were all reduced (***$P < 0.001$). In addition, such reduction was more significant in the GPRD group, mainly due to the targeted recognition of activated macrophages by GPRD NPs.

Inhibition of Foam Cell Formation and Oxidation-Induced Apoptosis by GPRD NPs in Activated RAW264.7 Cells

The continuous accumulation of ROS and inflammatory cytokines in atherosclerotic vulnerable plaque areas can aggravate the injury of endothelial cells and the expression of chemokines. In addition, it can also promote the expression of SR-A in macrophages and its own activation, resulting in the acceleration of the intake of ox-LDL by macrophages and the formation of foam cells.[36–38] The above results indicated that GPRD NPs could reduce ROS in activated cells and reduce the release of inflammatory cytokines. Thus, we further studied the following influence of GPRD NPs on the inhibition of foam cell formation and oxidation-induced apoptosis in activated RAW264.7 cells. As shown in Figure 3F, with LPS and ox-LDL treatment, the level of total cholesterol (TC) in cells was the highest (model group). But the TC levels went down in the presence of GPRD NPs and GPR NPs, indicating the inhibition of ox-LDL uptake by NPs. Moreover, TC levels in the GPRD NPs group were even lower than the non-targeted GPR NPs group due to the target of DS (***$P < 0.001$). Subsequently, the formation of foam cells was further compared by Oil Red O staining (ORO). Similarly, without LPS activation, few foam cells were formed in the control group even with ox-LDL incubation (Figure 3G and H). However, a large number of foam cells were observed in the model group (LPS + ox-LDL treatment), which was reduced in the presence of GPR NPs and GPRD NPs. The fewer foam cells in GPRD NPs group showed that GPRD NPs had a strong role in the inhibition of cellular internalization of ox-LDL and foam cell formation with the help of DS.

In atherosclerotic plaques, oxidative stress induced by ROS can promote the apoptosis of cells. Then, the necrotic core of the plaque becomes larger and the plaque is prone to rupture. Thus, ROS-scavenging by GPRD NPs might inhibit macrophage apoptosis. Apoptosis detection kit and flow cytometry were used to determine whether GPRD NPs could inhibit the apoptosis of macrophage induced by H_2O_2. As shown in Figure 3I, with 200 μM H_2O_2 injury for 24 h, about 27.4% of the RAW264.7 cells were apoptotic (model group), while only about 10.69% of the untreated cells were apoptotic (control group). However, with GPRD NPs or GPR NPs pre-intervention, the apoptosis rates induced by H_2O_2 were inhibited to be 14.91% and 21.35%, respectively. The results indicated that GPRD NPs could effectively inhibit macrophage apoptosis induced by peroxidation.

Targeted Dual-Modality Imaging for Activated RAW264.7 Cells

Atherosclerotic plaques are easy to be ignored due to their hidden early clinical manifestations. Thus, it is more necessary to identify early vulnerable lesions through the combination of multimodal imaging technology. At present, MRI and fluorescence imaging are widely used in AS.[39] MRI is used to obtain the anatomical structure of the diseased blood vessels. Meanwhile, the nature and composition of plaque are preliminarily analyzed. The molecular and cellular information can be obtained by fluorescence imaging with its high sensitivity. The advantages of bimodal imaging are integrated to provide a more accurate imaging mode for vulnerable plaque.

Before we applied GPRD NPs for targeted dual-modality imaging in vitro, an MTT assay was first performed to assess their cytotoxicity against RAW264.7 and HUVEC cells. As shown in Figure 4A, even at a high concentration of 400 μg/mL, more than 90% of the cells still survived after 24 h incubation with GPRD NPs for both RAW264.7 and HUVEC cells, suggesting the low toxicity and excellent biocompatibility of the prepared GPRD NPs ($P_{Raw264.7}$ =0.144 > 0.05, P_{HUVEC} =0.828 > 0.05). Then,

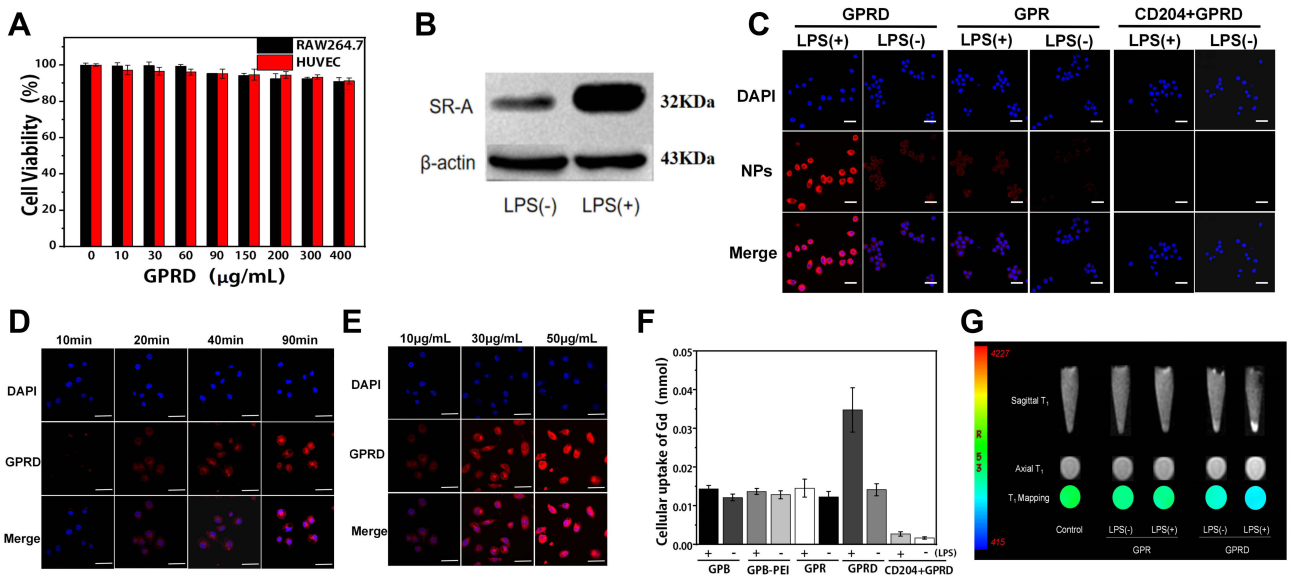

Figure 4 (**A**) Cell viability of RAW264.7 cells and HUVEC cells after exposure to various concentrations of GPRD NPs, determined by MTT assay. (**B**) Detection of the expression of SR-A in LPS activated macrophages. (**C**) The CLSM images of activated RAW 264.7 cells and untreated RAW264.7 cell incubated with GPR NPs, GPRD NPs or GPRD NPs with CD204 antibody pre-treated for 20 min. The cell nucleus was strained by DAPI. The CLSM images of activated RAW264.7 cells treated with different GPRD NPs concentrations (**D**) and different times (**E**). (**F**) The quantitative analysis of Gd in RAW264.7 cells with or without LPS stimulation after incubation with GPB, GPB-PEI, GPR, GPRD or CD204+GPRD NPs. (**G**) T_1-weighted and T_1 mapping image of LPS activated RAW264.7 cells and unactivated RAW264.7 cells incubated with GPR NPs or GPRD NPs. In CLSM images, the red color emissions were from NPs and blue color emissions were from cell nucleus. scale bar = 50 μm.

we used LPS to induce macrophage activation and evaluated the expression of SR-A in activated macrophages by Western Blot assay. As shown in Figure 4B, compared with unactivated macrophages, LPS-treated macrophages were activated and over-expressed SR-A strongly, showing the potential of SR-A as a target to recognize activated macrophages.

Then, the targeting ability of GPRD NPs towards activated and unactivated RAW264.7 cells was evaluated using CLSM. As shown in Figures 4C and S2a, there was strong red fluorescence from GPRD NPs in LPS activated cells and weak red fluorescence from GPR NPs. However, for the unactivated RAW264.7 cells, only a faint red fluorescence could be observed in cells no matter in the presence of GPRD NPs or GPR NPs, indicating the observed red fluorescence might come from the up-expressed SR-A on the cell surface of activated RAW264.7 after LPS treatment and the presence of targeting molecule, DS in GPRD NPs. The fluorescence imagings of RAW264.7 cells in the CD204 + GPRD NPs group with or without LPS treatment further testified this conclusion. With CD204 antibody pre-incubation, almost no red fluorescence could be observed even with LPS treatment and GPRD NPs binding, indicating that SR-A was critical for the specific binding of GPRD NPs with RAW264.7 cells. Furthermore, the red fluorescence emissions were time- and dose-dependent on GPRD NPs (Figures 4D, E, S2b and S2c). To further systematically study the specific binding of different state of NPs, GPB, GPB-PEI, GPR, GPRD or CD204 + GPRD NPs were incubated with RAW264.7 cells (LPS-/+), and the internalized Gd amount in treated cells was determined by ICP-MS. As shown in Figure 4F, the modification of PEI and Rd displayed almost no impact on the cellular uptake of GPB. However, in the presence of DS, the amount of GPRD in LPS-treated RAW264.7 cells was increased significantly, which was then strongly inhibited by CD204 antibody blocking, showing that the detected Gd in cells came from the SR-A mediated cellular uptake of GPRD NPs. Hence, the above results indicated that the DS-targeted GPRD NPs were more easily recognized and swallowed by activated RAW264.7 cells to be visualized by fluorescence imaging in vitro.

Later, the target MR imaging ability of GPRD NPs towards activated RAW264.7 cells was also evaluated by a 3.0T MR scanner. DS as the target molecules could selectively bind to SR-A, which overexpressed in activated RAW264.7 cells. Similar to the results of fluorescence imaging, a stronger signal intensity was observed in activated cells than that in unactivated cells after incubation with GPRD NPs (***$P < 0.001$) (Figures 4G, S2d and S2e). Nevertheless, for GPR NPs incubation, weak MRI signal was observed both in unactivated and activated RAW264.7 cells, showing the excellent targeted MRI ability of GPRD NPs towards activated RAW264.7 cells.

In vivo Safety Evaluation

The above behaviors of GPRD NPs as fluorescence/MR imaging agent and inhibition of AS related process in vitro encouraged us to explore their recognition and treatment of AS in vivo. Thus, in vivo safety was first evaluated. Blood compatibility is an important safety index of nanoparticles. Mice blood was collected to study the blood compatibility of GPRD NPs. Visual hemolysis images showed no obvious hemolysis with different concentrations of GPRD NPs and no significant difference in OD values between the GPRD NPs group and the negative control group (Figure S3a), indicating the good blood biocompatibility of GPRD NPs.

Then, the in vivo safety was systematically tested by H&E staining of major organs, blood biochemical analysis, and routine blood analysis. As shown in Figure S3b, histological analysis of major organs collected at 1st, 7th, and 21st day post-injection of GPRD NPs was performed to determine the biocompatibility of GPRD NPs in vivo. Compared with the control group, no significant inflammation or damage was observed in the major organs of the mice injected with GPRD NPs at all time points. For routine blood indexes and blood biochemical indexes analysis, no significant difference between GPRD NPs groups (1d, 7d, and 21d groups) and the control group in all common used indicators ($P_{AST} = 0.992 > 0.05$, $P_{ALB} = 0.228 > 0.05$, $P_{BUN} = 0.438 > 0.05$, $P_{CR} = 0.612 > 0.05$, $P_{ALT} = 0.159 > 0.05$, $P_{MCV} = 0.612 > 0.05$, $P_{HGB} = 0.297 > 0.05$; $P_{TP} = 0.378 > 0.05$, $P_{RBC} = 0.861 > 0.05$, $P_{WBC} = 0.529 > 0.05$, $P_{PCT} = 0.164 > 0.05$, $P_{MCH} = 0.676 > 0.05$), suggesting the acceptable in vivo safety of GPRD NPs (Figure S3c).

After 8 weeks of a high-fat diet, the ApoE -/- mice were intervented with saline, GPR NPs or GPRD NPs from week 9 (Figure 5A). The weights of mice were measured once a week and no significant difference was observed among the mice in all groups (Figure S4a), indicating that GPRD NPs had no significant effect on the bodyweight of mice. All of these data suggested the good biocompatibility and safety of GPRD NPs for the diagnosis and treatment of AS vulnerable plaques.

In vivo Targeted Dual-Modality Imaging of Vulnerable Plaques

After 8 weeks of a high-fat diet, Oil Red O staining of the aorta of ApoE-/- mice was first performed to show the well-developed atherosclerotic plaques. As shown in Figure 5B, a large number of Oil Red O stained area was observed in the collected thoracic aortas, showing the successful model construction. Immunofluorescence results showed that the pink fluorescence-labeled SR-A was significantly expressed in the plaque area of the thoracic aorta, confirming the presence of vulnerable plaques in our constructed ApoE -/- mice (Figure 5B), which was further verified by flow cytometry. As shown in Figure S4b, 67.6% of the cells in atherosclerotic lesions were CD204-positive while that was only 6.62% for the control group. The difference between the two groups was statistically significant (***$P < 0.001$). Then, we tried to realize the targeted MR and fluorescence imaging of ApoE-/- mice bearing vulnerable plaques with GPRD NPs. The mice were divided into two groups and injected with GPRD NPs or GPR NPs via tail vein, respectively. MR images were collected at different time points pre- and post-injection of NPs using a 3.0 T MR scanner. As shown in Figure 5C and D, the T_1 signal-to-noise ratio in vulnerable plaque brightened after 30 min injection of NPs, and then gradually increased to the maximum intensity at 2 h. Subsequently, the ratio gradually decreased over time within 24 hours. Moreover, the ratio in the vulnerable plaques of the GPRD NPs group was higher than that in the GPR NPs group, displaying the stronger targeting ability of GPRD NPs to vulnerable plaques. Besides, the accumulation of GPRD NPs and GPR NPs in the gallbladder with the time passing by, indicating their possible excretion route through the hepatobiliary system (Figure S4c-d), which was in accordance with the literature determined by the sizes of nanomaterials.[40,41]

Furthermore, after intravenous injection of GPRD NPs or GPR NPs 2 hours later, the isolated entire aorta showed significant fluorescence in the aortic arch and thoracoabdominal aorta in the GPRD NPs group (Figures 5E and S5a). However, the fluorescence emission in the aorta in the GPR NPs group was much weaker (***$P < 0.001$). Subsequently, the fluorescence emissions in the heart, liver, spleen, lung, and kidney were carried out and the strongest fluorescence was observed in the gallbladders in both NPs groups (Figure S5b-c), indicating the possible clearance route of the NPs by the hepatobiliary system once again.

The targeting ability of GPRD NPs against vulnerable plaques was further confirmed by immunofluorescence analysis. ApoE-/- mice bearing vulnerable plaques in two groups were injected with GPRD NPs or GPR NPs, respectively. Two hours later, the immunofluorescence analysis was performed in the thoracic aorta. It was showed

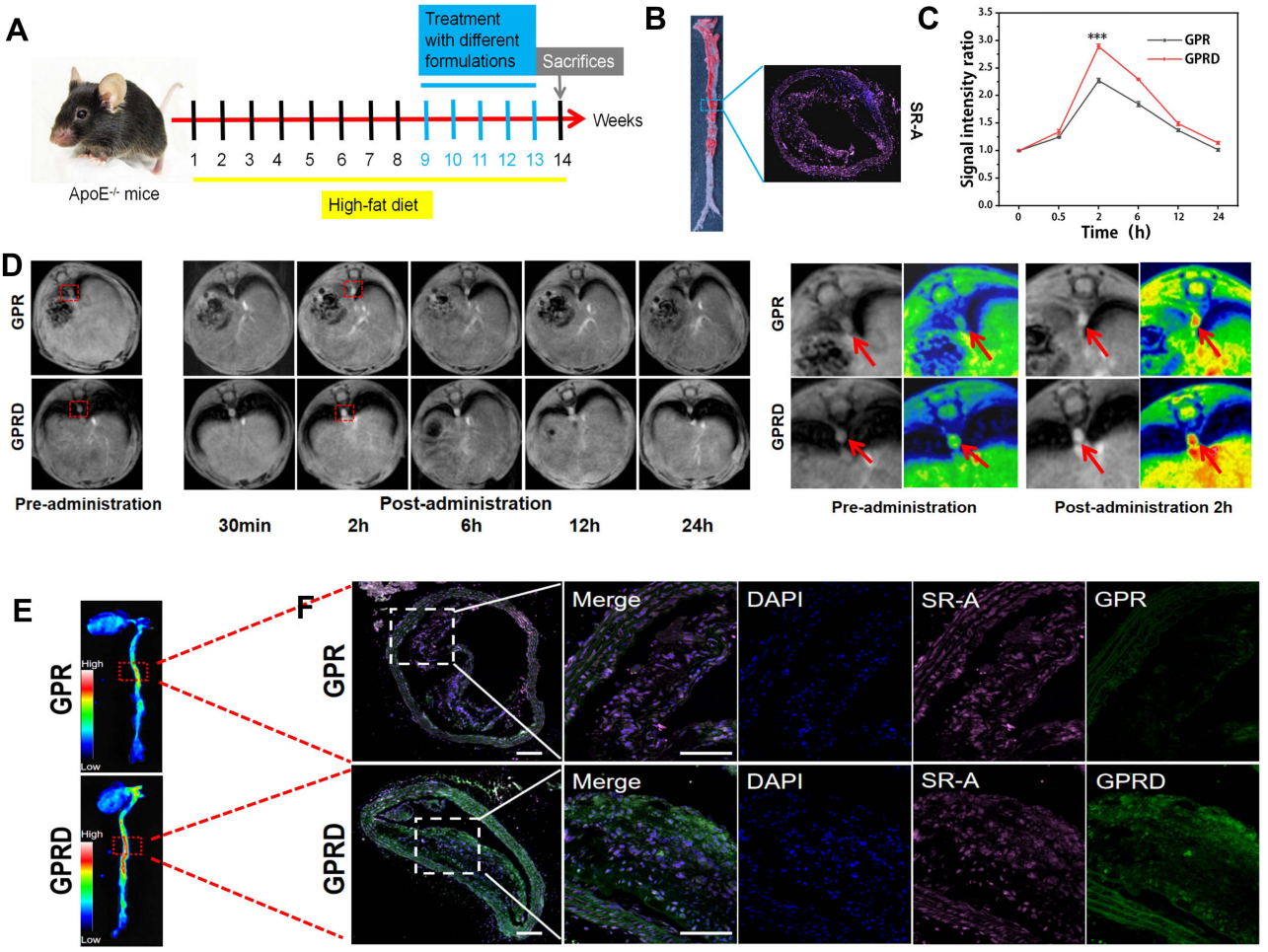

Figure 5 (**A**) Schematic illustration of atherosclerotic mouse model development and treatment with various formulations. (**B**) The aorta oil red O staining in the atherosclerotic model mice and the expression of SR-A in vulnerable plaque (pink: SR-A and blue: DAPI). (**C** and **D**) MR imaging of atherosclerotic model mice aorta plaque pre-injection and after injection of GPR or GPRD NPs at different time point and quantitative analysis of T_1 signal-to-noise ratio. The magnification T_1-weighted and pseudo-color images of plaque were also provided in d. (**E**) Fluorescence imaging of atherosclerotic model mice aorta plaque after injection of GPR or GPRD NPs at 2h. (**F**) Images of colocalization between GPR or GPRD NPs and SR-A in vulnerable plaque post-injection for 2h (scale bar =100 μm). ***$P < 0.001$.

that SR-A was abundant in the vulnerable plaque area, and the colocalization of GPRD NPs with SR-A could be found in the vulnerable plaque area (Figures 5F and S5d). The accumulated GPRD NPs in the SR-A region was much higher than GPR NPs, demonstrating the better targeting ability of GPRD NPs to SR-A in vulnerable plaques.

In vivo Targeted Treatment of Vulnerable Plaques

Afterward, we investigated the therapeutic effect of GPRD NP in vivo. ApoE -/- mice were randomly divided into four groups: control group (normal diet for mice without treatment), model group, GPRD NPs group, and GPR NPs group. After 2 months of high-fat diet, the latter three groups were given saline, GPRD NPs, and GPR NPs twice a week for 5 weeks, respectively. After 5 weeks, all the aortas were collected and stained with Oil-red O staining. A lower ORO-positive region was found in the control group and the highest ORO-positive region was found in the model group (Figure 6A). Especially, the ORO-stained regions of aortas in the GPRD NPs and GPR NPs group were significantly smaller than those of the model group, and the smallest ORO-stained region was observed in the GPRD NPs group. Further quantitative analysis was performed and the plaque areas in the control group, model group, GPR and GPRD-treated mice were 10.2 ± 1.4%, 44.5 ± 3.0%, 35.9 ± 1.7%, and 24.1 ± 0.9%, respectively (Figure S5e). The results suggested that GPRD NPs can efficaciously attenuate the development of AS.

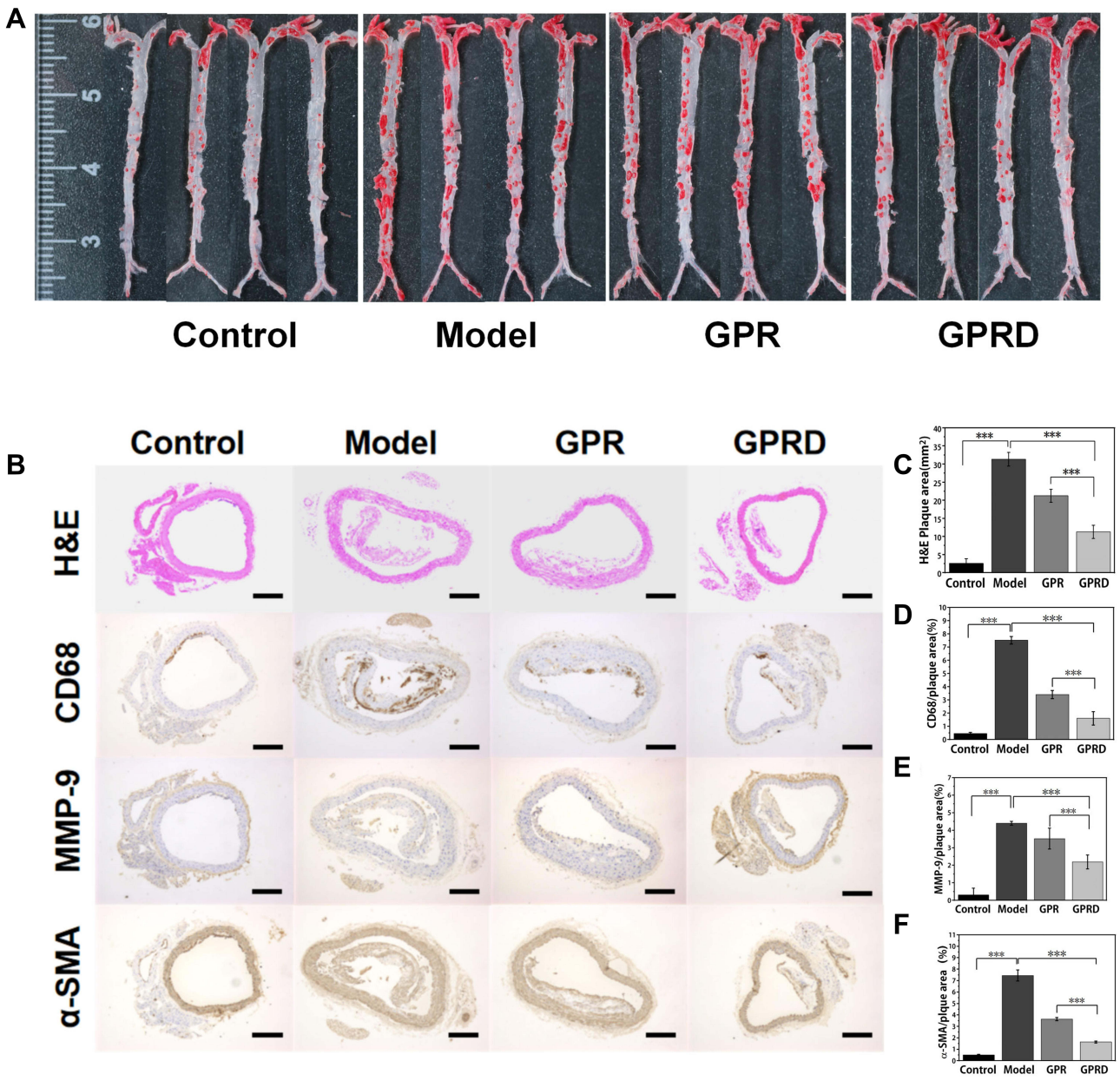

Figure 6 (**A**) ORO-stained aorta tissues collected from atherosclerotic mice after treatment with various formulations. (**B-F**) Representative photographs and quantitative analysis of thoracic aorta sections stained by H&E, CD68 antibody, MMP-9 antibody, and α-SMA antibody after treatment with various formulations (scale bar = 200 μm, ***$P < 0.001$). Control: mice fed with normal diets without treatment. Model: mice fed with high-fat diets and treated with normal saline.
Abbreviations: GPR, mice fed with high-fat diets and treated with GPR NPs; GPRD, mice fed with high-fat diets and treated with GPRD NPsï.

The area of plaque and the stability of plaque were the two main aspects to evaluate the effectiveness of treatment for AS. Thus, histological and immunohistochemical analyses of atherosclerotic plaques in the thoracic aorta were performed (Figure 6B). H&E staining showed that the plaque was the largest in the model group among all the groups (Figure 6C). GPR NPs and GPRD NPs could reduce the plaque area with a better effect in the GPRD group (***$P < 0.001$). This result indicated that GPRD NPs could effectively reduce the plaque area, which was consistent with the results of Oil-red O staining of the whole aortas. The infiltration of macrophages was positively correlated with the development of vulnerable plaques and the degradation of extracellular matrix and collagen by matrix metalloproteinases could accelerate the formation of vulnerable plaques. Thus, we chose CD68 and MMP-9 to evaluate the number of macrophages and the expression of matrix metalloproteinases in plaques after therapy. The results showed that GPRD NPs could effectively reduce the number of macrophages and the expression of MMP-9 in aortic plaques (Figure 6D and E). Smooth muscle cells

were the main components in AS plaques. α-SMA (smooth muscle cell labeling) immunohistochemical analysis was performed on aortic sections of mice from different groups. As shown in Figure 6F, a large number of smooth muscle cells were distributed in AS plaques in the model group and GPR NPs group, which was significantly reduced in the plaque of the GPRD NPs group. The experimental results showed that GPRD NPs could effectively prevent the progression of AS and played a vital role in the treatment and stabilization of vulnerable plaques.

Conclusion

In this study, integrated MR/fluorescence dual-modal imaging and therapeutic nanoparticles have been constructed to target and treat AS vulnerable plaques. Based on the MR and fluorescence imaging ability of GPB and Rd, the nano-enzyme capability of GPB as well as the targeting ability of DS, the fabricated GPRD NPs displayed successfully in vivo imaging of AS vulnerable plaque and the inhibition of plaque progress. The ROS-scavenging strategy to inhibit the AS plaque progress and stabilize the vulnerable plaques possesses promising potentials for AS treatment because of the important role of ROS in the formation and progress of AS. The ROS clearance brought a series of ROS-related changes, such as the reduction of oxidative stress, inflammation, apoptosis, and the formation of macrophage-derived foam cells, which all favored the therapy of AS plaque. It should be mentioned that such MRI and therapy both came from the GPB NPs themselves without extra drug loading, which simplified the preparation of nanocomplex. The dual-modal imaging and therapy of AS vulnerable plaques by our fabricated GPRD NPs might promote the early identification and treatment of AS plaques. In the future, it will be intriguing to employ more NIR-II fluorescent molecules for in vivo imaging without the dissection of thoracic aortas, favoring the clinical translation more easily. Furthermore, with the development of GPB with mesoporous structure, synergistic therapy of AS would be realized to face the complex pathological process of AS.

Acknowledgments

This work was supported by the National Natural Science Foundation of China (8217071424), the Natural Science Foundation of Jiangsu Province (BK20221391), Qing Lan Project, the Peak of Six Talents of Jiangsu Province (WSN-112), Jiangsu Provincial Medical Youth Talent (QNRC2016776), Six one project of Jiangsu Province (LGY2018083). Postgraduate Research & Practice Innovation Program of Jiangsu Province (KYCX21_2737, KYCX21_2724 and KYCX20_2448).

Disclosure

The authors report no conflicts of interest in this work.

References

1. Khambhati J, Engels M, Allard-Ratick M, et al. Immunotherapy for the prevention of atherosclerotic cardiovascular disease: promise and possibilities. *Atherosclerosis*. 2018;276:1–9.
2. Roth GA, Johnson C, Abajobir A, et al. Global, regional, and national burden of cardiovascular diseases for 10 causes, 1990 to 2015. *J Am Coll Cardiol*. 2017;70(1):1–25.
3. Wang J, Wu M, Chang J, et al. Scavenger receptor-AI-targeted ultrasmall gold nanoclusters facilitate in vivo MR and ex vivo fluorescence dual-modality visualization of vulnerable atherosclerotic plaques. *Nanomedicine*. 2019;19:81–94.
4. Tong W, Hui H, Shang W, et al. Highly sensitive magnetic particle imaging of vulnerable atherosclerotic plaque with active myeloperoxidase-targeted nanoparticles. *Theranostics*. 2021;11(2):506–521.
5. Ma S, Motevalli SM, Chen J, et al. Precise theranostic nanomedicines for inhibiting vulnerable atherosclerotic plaque progression through regulation of vascular smooth muscle cell phenotype switching. *Theranostics*. 2018;8(13):3693–3706.
6. Kim M, Sahu A, Hwang Y, et al. Targeted delivery of anti-inflammatory cytokine by nanocarrier reduces atherosclerosis in Apo E-/- mice. *Biomaterials*. 2020;226:119550.
7. Kim M, Sahu A, Kim GB, et al. Comparison of in vivo targeting ability between cRGD and collagen-targeting peptide conjugated nano-carriers for atherosclerosis. *J Control Release*. 2018;269:337–346.
8. Stocker R, Keaney JF. Role of oxidative modifications in atherosclerosis. *Physiol Rev*. 2004;84(4):1381–1478.
9. Mittal M, Siddiqui MR, Tran K, et al. Reactive oxygen species in inflammation and tissue injury. *Antioxid Redox Signal*. 2014;20(7):1126–1167.
10. Yang B, Chen Y, Shi J. Reactive Oxygen Species (ROS)-based nanomedicine. *Chem Rev*. 2019;119(8):4881–4985.
11. Liang M, Yan X. Nanozymes: from new concepts, mechanisms, and standards to applications. *Acc Chem Res*. 2019;52(8):2190–2200.
12. Jiang D, Ni D, Rosenkrans ZT, et al. Nanozyme: new horizons for responsive biomedical applications. *Chem Soc Rev*. 2019;48(14):3683–3704.
13. Zhou Y, Liu B, Yang R, et al. Filling in the gaps between nanozymes and enzymes: challenges and opportunities. *Bioconjug Chem*. 2017;28(12):2903–2909.

14. Zhang W, Hu S, Yin JJ, et al. Prussian blue nanoparticles as multienzyme mimetics and reactive oxygen species scavengers. *J Am Chem Soc*. 2016;138(18):5860–5865.
15. Zuo D, Tan B, Jia G, et al. A treatment combined Prussian blue nanoparticles with low-intensity pulsed ultrasound alleviates cartilage damage in knee osteoarthritis by initiating PI3K/Akt/mTOR pathway. *Am J Transl Res*. 2021;13(5):3987–4006.
16. Bai H, Kong F, Feng K, et al. Prussian Blue nanozymes prevent anthracycline-induced liver injury by attenuating oxidative stress and regulating inflammation. *ACS Appl Mater Interfaces*. 2021;13(36):42382–42395.
17. Zhang DY, Liu H, Zhu KS, et al. Prussian blue-based theranostics for ameliorating acute kidney injury. *J Nanobiotechnology*. 2021;19(1):266.
18. Zhang K, Tu M, Gao W, et al. Hollow Prussian blue nanozymes drive neuroprotection against ischemic stroke via attenuating oxidative stress, counteracting inflammation, and suppressing cell apoptosis. *Nano Lett*. 2019;19(5):2812–2823.
19. Zhao J, Cai X, Gao W, et al. Prussian Blue nanozyme with multienzyme activity reduces colitis in mice. *ACS Appl Mater Interfaces*. 2018;10 (31):26108–26117.
20. Zhao J, Gao W, Cai X, et al. Nanozyme-mediated catalytic nanotherapy for inflammatory bowel disease. *Theranostics*. 2019;9(10):2843–2855.
21. Wang Z, Long Y, Fan J, et al. Biosafety and biocompatibility assessment of Prussian blue nanoparticles in vitro and in vivo. *Nanomedicine*. 2020;15 (27):2655–2670.
22. Dumani DS, Cook JR, Kubelick KP, et al. Photomagnetic Prussian blue nanocubes: synthesis, characterization, and biomedical applications. *Nanomedicine*. 2020;24:102138.
23. Yang M, Ding J, Feng X, et al. Scavenger receptor-mediated targeted treatment of collagen-induced arthritis by dextran sulfate-methotrexate prodrug. *Theranostics*. 2017;7(1):97–105.
24. You DG, Saravanakumar G, Son S, et al. Dextran sulfate-coated superparamagnetic iron oxide nanoparticles as a contrast agent for atherosclerosis imaging. *Carbohydr Polym*. 2014;101:1225–1233.
25. Zhao Y, Jiang C, He J, et al. Multifunctional dextran sulfate-coated reconstituted high density lipoproteins target macrophages and promote beneficial antiatherosclerotic mechanisms. *Bioconjug Chem*. 2017;28(2):438–448.
26. Cai X, Gao W, Zhang L, et al. Enabling Prussian blue with tunable localized surface plasmon resonances: simultaneously enhanced dual-mode imaging and tumor photothermal therapy. *ACS Nano*. 2016;10(12):11115–11126.
27. Yang Y, Jing L, Li X, et al. Hyaluronic acid conjugated magnetic Prussian Blue@quantum dot nanoparticles for cancer. *Theranostics*. 2017;7 (2):466–481.
28. Dou Y, Li X, Yang W, et al. PB@Au core-satellite multifunctional nanotheranostics for magnetic resonance and computed tomography imaging in vivo and synergetic photothermal and radiosensitive therapy. *ACS Appl Mater Interfaces*. 2017;9(2):1263–1272.
29. Wang Y, Zhang K, Li T, et al. Macrophage membrane functionalized biomimetic nanoparticles for targeted anti-atherosclerosis applications. *Theranostics*. 2021;11(1):164–180.
30. Mansouri H, Gholibegloo E, Mortezazadeh T, et al. A biocompatible theranostic nanoplatform based on magnetic gadolinium-chelated poly-cyclodextrin: in vitro and in vivo studies. *Carbohydr Polym*. 2021;254:117262.
31. Li J, You J, Dai Y, et al. Gadolinium oxide nanoparticles and aptamer-functionalized silver nanoclusters-based multimodal molecular imaging nanoprobe for optical/magnetic resonance cancer cell imaging. *Anal Chem*. 2014;86(22):11306–11311.
32. Vázquez-González M, Torrente-Rodríguez RM, Kozell A, et al. Mimicking peroxidase activities with Prussian blue nanoparticles and their cyanometalate structural analogues. *Nano Lett*. 2017;17(8):4958–4963.
33. Zhou J, Li M, Hou Y, et al. Engineering of a nanosized biocatalyst for combined tumor starvation and low-temperature photothermal therapy. *ACS Nano*. 2018;12(3):2858–2872.
34. Zhou T, Liang X, Wang P, et al. A Hepatocellular carcinoma targeting nanostrategy with hypoxia-ameliorating and photothermal abilities that, combined with immunotherapy, inhibits metastasis and recurrence. *ACS Nano*. 2020;14(10):12679–12696.
35. Wang P, Kankala RK, Chen B, et al. Cancer cytomembrane-cloaked Prussian blue nanoparticles enhance the efficacy of mild-temperature photothermal therapy by disrupting mitochondrial functions of cancer cells. *ACS Appl Mater Interfaces*. 2021;13(31):37563–37577.
36. Lusis AJ. Atherosclerosis. *Nature*. 2000;407(6801):233–241.
37. Steinberg D. Lipoproteins and the pathogenesis of atherosclerosis. *Circulation*. 1987;76(3):508–514.
38. Ference BA, Kastelein JJP, Catapano AL. Lipids and lipoproteins in 2020. *JAMA*. 2020;324(6):595–596.
39. Vigne J, Thackeray J, Essers J, et al. Current and emerging preclinical approaches for imaging-based characterization of atherosclerosis. *Mol Imaging Biol*. 2018;20(6):869–887.
40. Choi HS, Liu W, Misra P, et al. Renal clearance of quantum dots. *Nat Biotechnol*. 2007;25(10):1165–1170.
41. Yu M, Zheng J. Clearance pathways and tumor targeting of imaging nanoparticles. *ACS Nano*. 2015;9(7):6655–6674.